AGU PUBLICATIONS

Geophysical Research Letters

RESEARCH LETTER

10.1002/2017GL075744

Key Points:
- We detected inflation, likely due to magma, beneath Mount Etna's summit region
- During the inflation, we detected a new Slow Slip Event on the eastern flank of Mount Etna
- We construct a model of the inflation leading to the slow slip supported by stress and strain calculations

Supporting Information:
- Supporting Information S1

Correspondence to:
M. Mattia,
mario.mattia@ingv.it

Citation:
Bruno, V., Mattia, M., Montgomery-Brown, E., Rossi, M., & Scandura, D. (2017). Inflation leading to a Slow Slip Event and volcanic unrest at Mount Etna in 2016: Insights from CGPS data. *Geophysical Research Letters*, *44*. https://doi.org/10.1002/2017GL075744

Received 4 MAY 2017
Accepted 10 NOV 2017
Accepted article online 15 NOV 2017

©2017. American Geophysical Union. All Rights Reserved.

Inflation Leading to a Slow Slip Event and Volcanic Unrest at Mount Etna in 2016: Insights From CGPS Data

V. Bruno[1], M. Mattia[1], E. Montgomery-Brown[2], M. Rossi[1], and D. Scandura[1]

[1]Istituto Nazionale di Geofisica e Vulcanologia, Osservatorio Etneo, Catania, Italy, [2]California Volcano Observatory, United States Geological Survey, Menlo Park, CA, USA

Abstract Global Positioning System (CGPS) data from Mount Etna between May 2015 and September 2016 show intense inflation and a concurrent Slow Slip Event (SSE) from 11 December 2015 to 17 May 2016. In May 2016, an eruptive phase started from the summit craters, temporarily stopping the ongoing inflation. The CGPS data presented here give us the opportunity to determine (1) the source of the inflating body, (2) the strain rate parameters highlighting shear strain rate accumulating along NE Rift and S Rift, (3) the magnitude of the SSE, and (4) possible interaction between modeled sources and other flank structures through stress calculations. By analytical inversion, we find an inflating source 5.5 km under the summit (4.4 km below sea level) and flank slip in a fragmented shallow structure accommodating displacements equivalent to a magnitude M_w6.1 earthquake. These large displacements reflect a complex mechanism of rotations indicated by the inversion of CGPS data for strain rate parameters. At the scale of the volcano, these processes can be considered precursors of seismic activity in the eastern flank of the volcano but concentrated mainly on the northern boundary of the mobile eastern flank along the Pernicana Fault and in the area of the Timpe Fault System.

Plain Language Summary In this manuscript we provide a detailed analysis of a period of inflation at Mount Etna. During this inflation, a slow slip event occurred on Mount Etna's eastern flank. We model both the inflation phase and the slow slip event to investigate the sources and the possible relationships between these sources and the volcanic and seismic activity at Mount Etna.

1. Introduction

Since 2000, 35 Continuous GPS (CGPS) stations at Mount Etna operated by the INGV-OE (Istituto Nazionale di Geofisica e Vulcanologia, Osservatorio Etneo) (Figure 1) have provided information about the evolution, in time and space, of volcanic sources beneath the volcano (e.g., Aloisi et al., 2003, 2011; Bruno et al., 2012, 2016; Mattia et al., 2007). CGPS data (e.g., Figure 2) have been particularly useful for defining periods characterized by magmatic system dynamics (inflation/deflation) and detecting both the secular southeastward trend of the eastern flank of the volcano (e.g., Bonforte et al., 2011; Bruno et al., 2012) and the Slow Slip Events (SSE) that occasionally occur, mainly in the lower sector of the eastern flank (e.g., Mattia et al., 2015).

We studied a period of inflation at Mount Etna and the concurrent lower eastern flank SSE between 11 December 2015 and 17 May 2016. In particular, the velocity field, modeled through an analytical inversion (Figure 3 and supporting information), provides insights into two deformation mechanisms: a volcanic source approximately 4.4 km below sea level (bsl) (5.5 km below the mean CGPS station elevation) and a shallow, highly fragmented body accommodating SSE. We also mapped strain rate parameters to improve our understanding of ground deformation patterns around Mount Etna. Calculations show that during this inflation and concurrent SSE, strike-slip stresses on the Pernicana Fault (PF) are encouraged toward failure by flank SSE, suggesting the importance of flank SSEs at Mount Etna into seismic hazard assessments.

2. Volcano-Tectonic Setting

At Mount Etna volcano, NNW-SSE trending structures directly control magma ascent. This main structural system is also connected to a larger scale, WNW-ESE oriented, extensional regime (Monaco et al., 1997). The main tectonic features of Mount Etna are recognizable on the east and south-east flanks of the volcano, where there is morphological evidence of active faulting. The seismicity on the eastern flank of Mount Etna is characterized by diffuse shallow earthquakes (depth about 7 km bsl) and aseismic creep along

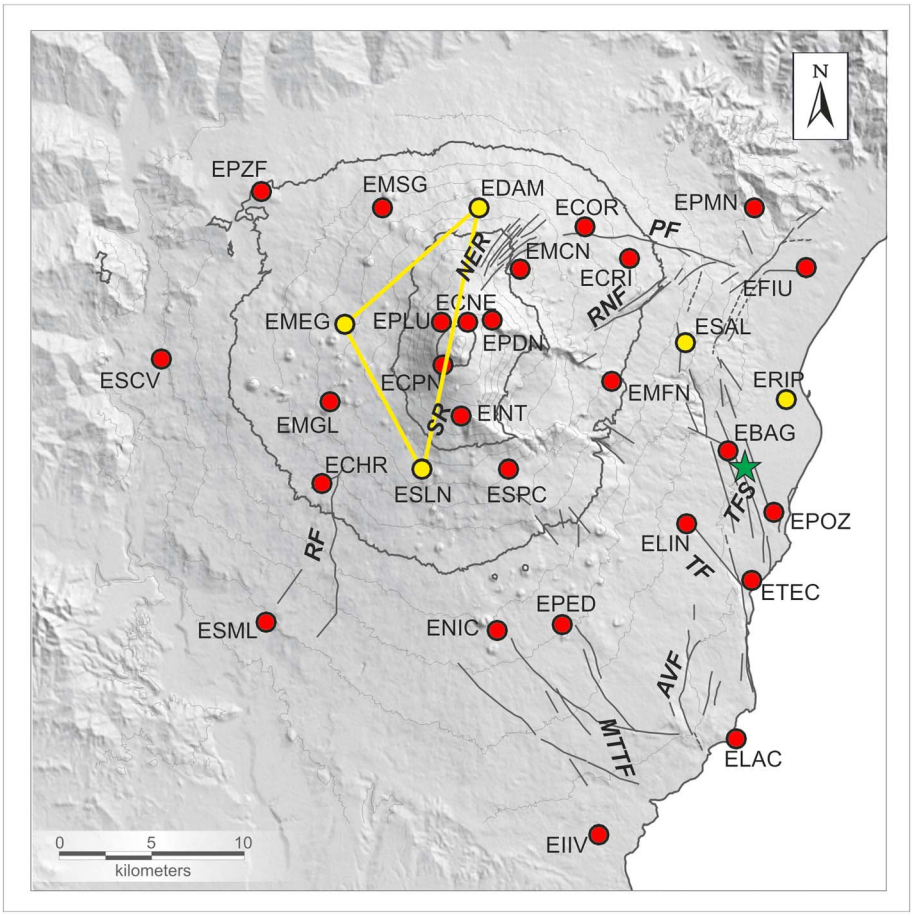

Figure 1. Maps of Mount Etna with the major faults and toponyms (NER: North-East Rift; SR: South Rift; TFS: Timpe Fault System; TF: Santa Tecla Fault; MTTFS: Mascalucia-Tremestieri-Trecastagni Fault System; AVF: Acicatena-Valverde Fault; PF: Pernicana Fault; RF: Ragalna Fault; and RNF: Ripe della Naca Fault). Red circles show locations of CGPS stations and those highlighted in yellow have time series shown in Figure 2. The yellow triangle delineates the boundary of the areal time series shown in Figure 2a and positional time series for ERIP and ESAL are shown in Figures 2b and 2c, respectively. The green star indicates the location of San Leonardello village.

some faults, which produces a typical secular trend of this flank toward the SE (Figure S1). In Figure 2 the acceleration of the secular southeastward motion of the eastern flank during the SSEs is shown. In this sense, investigation of the higher amplitude displacements during the SSEs can be considered as a proxy for a more general model of the instability of the Mount Etna's eastern flank, as the one proposed in Mattia et al. (2015).

Mattia et al. (2015) revealed the occurrence of SSE at Mount Etna and proposed that hot fluids from a recent inflation circulate at shallow depths (0–3 km bsl) beneath the highly fractured eastern flank and facilitate slip. This hypothesis was supported by the pre-SSE observations of seismicity, well water levels and geochemical data indicating the arrival of volcanic fluids, with the impermeable clay layer underlying Mount Etna's lavas trapping the fluids and increasing pressures.

3. Modeling of CGPS Data

The GPS data were processed for both position and velocity solutions (Table S1) using standard methods provided in the GAMIT/GLOBK software (Herring et al., 2006), then rotated into a published local reference frame (Palano et al., 2010; see supporting information for velocity data). From the analysis of the CGPS time series (Figure 2), we selected a time period where both inflation and accelerated flank slip are visible (11 December 2015 to 17 May 2016). Figure 2a shows the areal variation of the triangle linking CGPS stations EDAM, EMEG, and ESLN (Figure 1). Expansion or contraction of the triangle shows how the volcanic edifice underwent

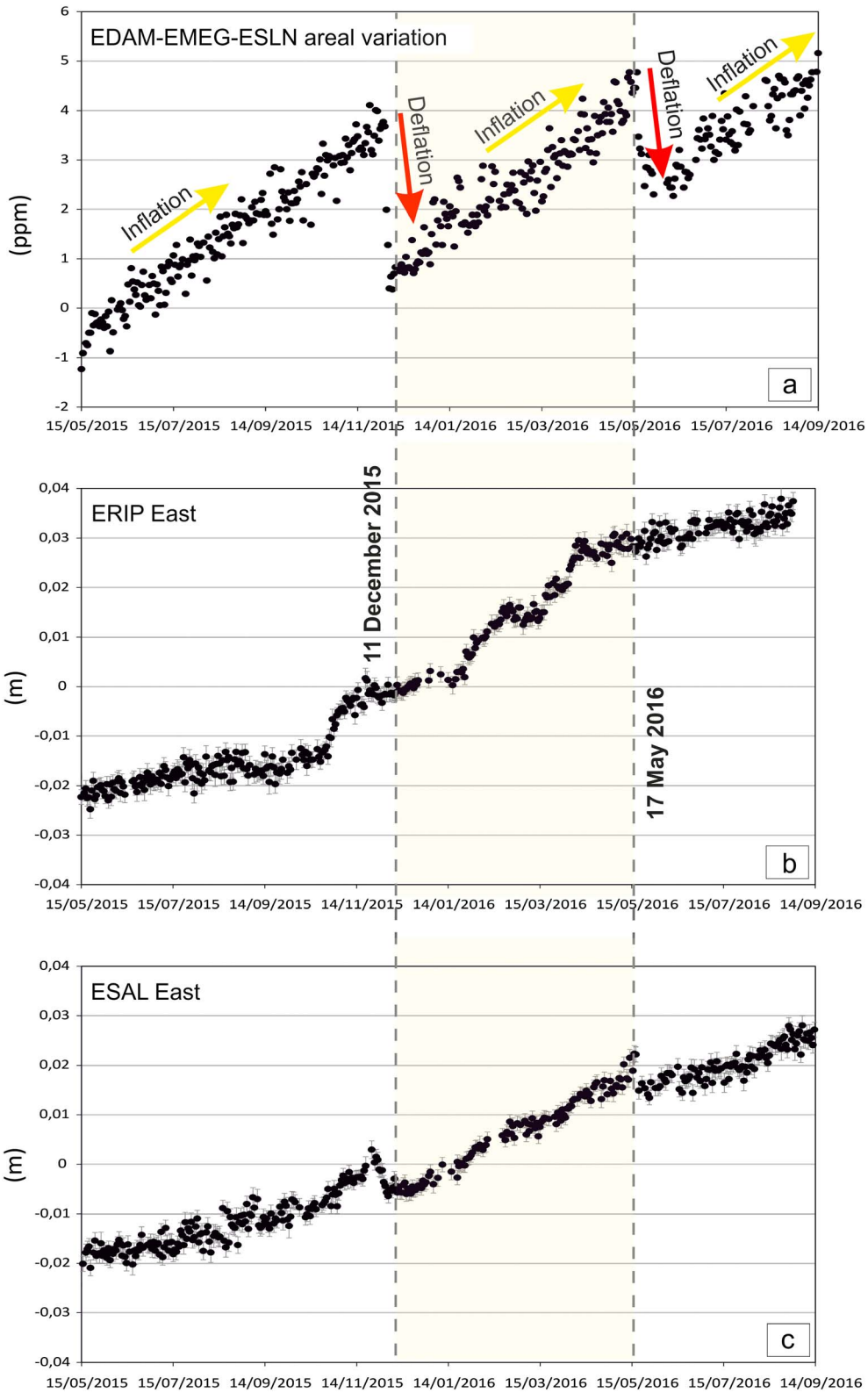

Figure 2. (a) Areal variation of the triangle EDAM-EMEG-ESLN; the time series evidences periods of dilatation, indicating inflation (yellow arrows), followed by sudden and clear contractions, during periods of deflations (red arrows) due to volcanic activity; (b, c) east components of the position time series of the ERIP and ESAL stations, respectively. The light yellow box delimited by vertical dotted gray lines indicates the period of ground deformation analyzed in this work (11 December 2015 to 17 May 2016).

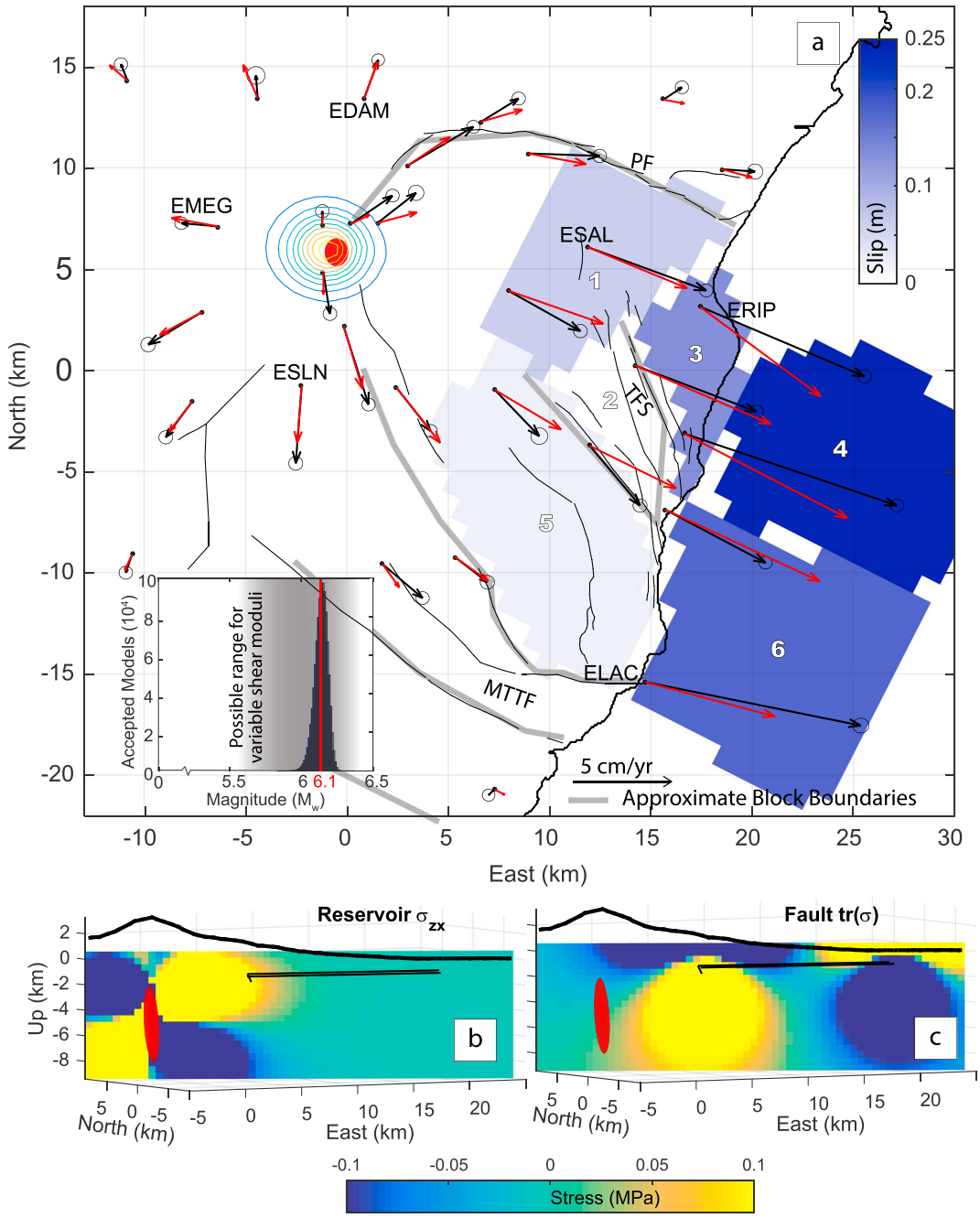

Figure 3. (a) Observed (black) and predicted (red) displacements for a combined inflation and flank slip model. Parameter distributions are presented in the supporting information, with slip location (white block numbers) corresponding to posterior distributions with the same numbers. The bull's-eye around Mount Etna's summit indicates the range of acceptable locations for the reservoir, while the red ellipse shows the preferred location and dimension. The intensity of the blue color indicates the magnitude of seaward slip. The origin of the local ENU (East, North, Up) coordinate system is longitude 15°, latitude 37.7°. Inset: Distribution of flank slip magnitudes for all accepted models computed from the integral of all slip in each model. The true lower limit based on the uniform input distributions of [0, 0.5] m/yr is a M_w0, but the lower limit of the axis was adjusted for visual clarity. The shaded area indicates a larger range in which the magnitude distribution could fall assuming a shear modulus from 0.5×10^{10} Pa (very small) to 7×10^{10} Pa (measured in lab samples but unrealistic for a model domain size of fractured basalts; see supporting information for details; Schultz, 1995). (b, c) Shear stresses in the direction of flank slip induced by the inflation, and conversely, the volumetric stresses produced by the trace of the stress tensor. Interactions between the reservoir and the SSE slip are not significant.

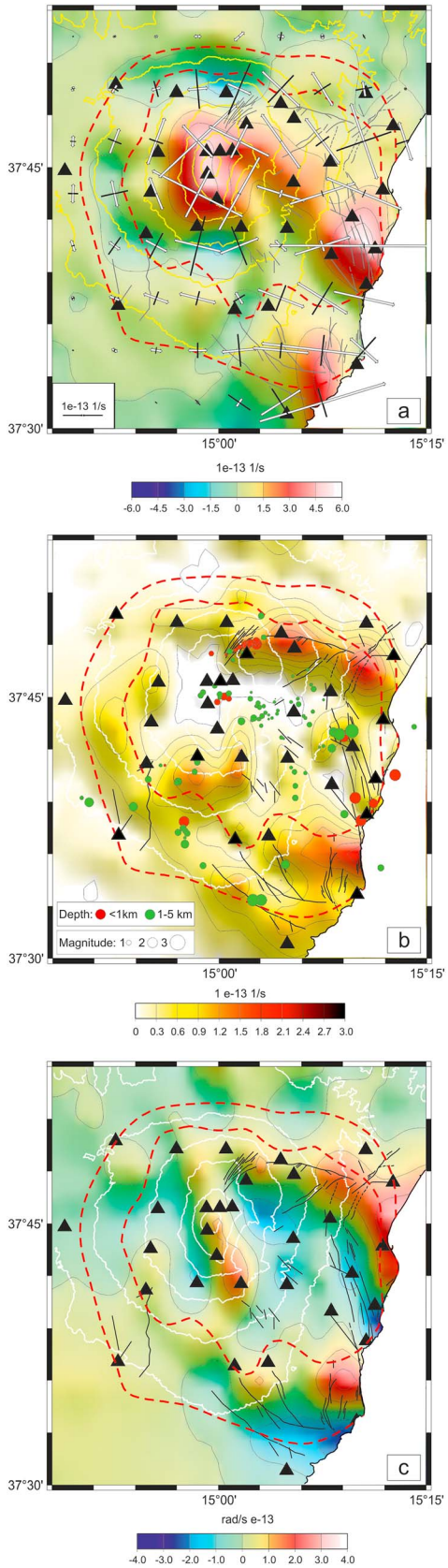

different phases of inflation and deflation during the selected time interval. In particular, the eruptive events that started on 2 December 2015 interrupted inflation of the volcanic edifice that began with the end of the 11–16 May 2015 Strombolian activity, when the NE portion of the 28 December 2014 fissure (Ferlito et al., 2017) issued a lava flow (Corsaro et al., 2017). Since 3 December 2015 a variety of eruptive phenomena involved the summit area (Corsaro et al., 2017) including paroxysmal episodes with strong lava fountains and eruptive columns up to about 14 km above sea level (asl), weak Strombolian activity followed by small lava flows and ash emissions. A new inflation episode started on 11 December 2015 and continued until 17 May 2016 (Figure 2a), when Strombolian activity, a lava fountain, and small lava flows (INGV-OE Internal report to DPC (Civil Protection Department), 2016) preceded a short deflation (Figure 2a).

Between 11 December 2015 and 17 May 2016, deformation of the CGPS stations shows a radial outward pattern (Figures 2a and 3) and the deformation of the lower eastern flank of Mount Etna accelerated eastward (Figures 2b, 2c, and 3). Since this acceleration period occurred without seismicity in the early phases nor any seismicity near the largest eastward displacements, we classified this acceleration as an SSE similar to prior SSEs (Mattia et al., 2015). Only in the final phase of this SSE (March–May 2016) localized seismic swarms occurred on the eastern slope of the volcano (see Figure 4b). The swarms occurred April 2016 on the lower eastern flank (M_{max} = 2.6), 8 May 2016 in Ragalna (M_{max} = 2.0), and 12–17 May 2017 in Mascalucia-Trecastagni (M_{max} = 2.0). On 31 March 2016, the road near San Leonardello (location noted in Figure 1) was damaged after an extremely shallow earthquake south of San Leonardello fault (Ml = 2.2). Other SSEs have been observed, and related to the earlier inflation phase leading to the eruptive activity of the first days of December 2015.

3.1. Model of Slow Slip and Inflation

In the model, we include the summit reservoir as an ellipsoidal source (Yang et al., 1988, updated by Cervelli (2013) in a linear elastic half-space (shear modulus $\mu = 3 \times 10^{10}$ Pa; Poisson's Ratio $\nu = 0.25$). The ellipsoidal source is described by the following eight parameters: source dimension, aspect ratio, dip, strike, east position (X), north position (Y), depth (Z), and volume change ΔV.

We also included the SSE as a nearly horizontal fault plane, but since the flank slip at Mount Etna occurs in cohesive blocks (Bonforte et al., 2011;

Figure 4. (a) Areal strain rates and principal axes of the average strain rates. Extensional strain rates are indicated by open arrows, while compressional strain rates are indicated by solid arrows; (b) magnitude of geodetic shear strain rate associated with the pure strike-slip component of the strain tensor field (equal magnitudes of compression and extension principal axes) and epicentral map and depth distribution of shallow earthquakes recorded in the study area during the analyzed period (11 December 2015 to 17 May 2016, Gruppo Analisi Dati Sismici, 2016, http://sismoweb.ct.ingv.it/maps/eq_maps/sicily/); (c) geodetic rotation rates. Negative values indicate clockwise rotations while positive values represent counterclockwise rotations. Areas with 50% (inner) and 70% (outer) strain rate field resolution levels (Kreemer et al., 2000) are marked with red dashed lines in each figure.

Table 1
Parameters From the MCMC Simulation Including 10 Million Accepted Models With a Final Acceptance Rate 19%

Parameter	Description	95% low	68% low	Mode	Best	68% high	95% high
a (m)	Vertical semimajor axis	556.5	893.1	1,465	1,239	2,601	2,942
$\mathrm{Log}_{10}[a/b]$ (a/b)	Ratio of major to minor axes	0.01 (1.02)	0.09 (1.23)	0.17 (1.47)	0.45 (2.8)	0.49 (3.09)	0.58 (3.8)
Dip (deg)	90° is vertical; 0° and 180° are horizontal	7.1	46.2	91.2	71.8	1,336	172.7
Strike (deg)	Clockwise from 0° North	8.8	69.4	135	142.9	309.1	351.3
X (m)	East position relative to [Lon: 15, Lat: 37.7]	−3,945	−2,414	−810	−1,073	350.6	1,978
Y (m)	North position relative to [Lon: 15, Lat: 37.7]	3,644	4,819	6,130	6,555	7,265	8,672
Z (m)	Depth below mean station elevation (1,147 m)	−9,885	−9,230	−8,170	−5,552	−5,896	−4,422
V (m^3/yr)	Volume change rate (positive implies inflation)	0.6×10^7	0.9×10^7	1.3×10^7	1.2×10^7	2.0×10^7	2.8×10^7
DS1 (m/yr)	Seaward slip rate on Patch 1	0.007	0.03	0.06	0.07	0.09	0.13
DS2 (m/yr)	Seaward slip rate on Patch 2	0.001	0.01	0.001	0.02	0.08	0.13
DS3 (m/yr)	Seaward slip rate on Patch 3	0.01	0.05	0.11	0.11	0.21	0.30
DS4 (m/yr)	Seaward slip rate on Patch 4	0.05	0.14	0.23	0.25	0.32	0.41
DS5 (m/yr)	Seaward slip rate on Patch 5	0.001	0.01	0.02	0.01	0.06	0.09
DS6 (m/yr)	Seaward slip rate on Patch 6	0.05	0.10	0.15	0.16	0.20	0.25

Note. Posterior distributions are available in the supporting information. The "Best" model implies maximum probability from the accepted models.

heavy gray lines in Figure 3), we simulate the blocks as follows. We modeled the SSE with planar elastic dislocations (Okada, 1985), subdivided into 1 km patches and extending across the eastern flank (similar to Mattia et al., 2015, and Palano, 2016). The major fault parameters (strike = 20°, depth = 1 km bsl, and dip = 179°; consistent with Palano, 2016) were determined from a prior SSE in the absence of inflation and then expanded to cover the eastern flank (Mattia et al., 2016). The fits to the vertical deformation measurements, and some notes on the limited influence of implementing a topographic correction following the methods of Williams and Wadge (1998), are provided in the supporting information. We simulate Mount Etna's flank blocks (Figure 3; Bonforte et al., 2011) by requiring the slip patches within each block to slip uniformly together, eliminating the need to smooth the slip or choose a smoothing weight; however, a smooth distributed model is also provided in the supporting information (Aster et al., 2012).

The parameter spaces, and particularly the uncertainties, of the inflation source and slip rates are explored through a Markov Chain Monte Carlo (MCMC) simulation following the methods of Anderson and Segall (2013). This MCMC analysis determines the uncertainties in the full set of eight ellipsoid parameters with six linear slip estimates from precomputed Green's functions (unit slip on each patch). The MCMC method uses the Metropolis-Hastings algorithm (Hastings, 1970; Metropolis et al., 1953) to test multiple hypothesis models generated from a stochastic process. In each of the simulations, we compute relative likelihoods and accept 10 million models. Each hypothesis is accepted if it improves on the previous model, but to ensure full sampling of the posterior parameter distributions a less likely model may also be accepted according to a random process. The step size of the random walk is adjusted such that the acceptance rate of models is maintained at about 15–25%. The ratio of major axis to minor axis (a/b) is sampled in log space because of the large solution differences between prolate and oblate ellipsoids. Prior distributions are assumed to be uniform between wide, but reasonable, bounds. The accepted model with the highest probability (lowest misfit) is chosen as the preferred model for discussion.

While summit inflation was ongoing from May 2015 to September 2016, a significant component of the volcano-wide deformation between 11 December 2015 and 17 May 2016 was from the eastward accelerated motion of CGPS stations on the eastern flank during an SSE. Here we present a combined model of the magma reservoir and eastern flank motion. An analysis of the summit source independently is available in the supporting information for comparison with previous work (e.g., Aloisi et al., 2011; Bruno et al., 2012, 2016).

The preferred reservoir (Table 1 and Figures 3 and S2) is a nearly vertical prolate ellipsoid under the summit with a vertical semidiameter (a) of 1.2 km with a log aspect ratio of 0.45 (a/b = 2.8). The preferred depth is about 5.5 km below the mean elevation of the stations (equivalent to ~4.4 km bsl), with a volume change rate of $12 \times m^3$/yr (total volume of 4.7×10^6 m^3 over the 158 days studied).

In this model, the posterior parameters of the ellipsoid remain similar to the summit-only model (see supporting information). Depth is the exception, for which the range is broader and permissive of deeper reservoirs

due to the model trying to accommodate the largest displacements on the eastern coast (deeper sources result in displacements at greater horizontal distances from the source; Segall, 2010). The deeper sources, however, result in misfits of the near-summit stations and the far-field western flank stations. Slip on each of the fault patches is allowed to range from 0 to 0.5 m/yr, with the optimal slip rate on the patches ranging up to 0.23 m/yr (on the order of 10^{-9} m/s for comparison with other studies). Some of the blocks are constrained by very few nearby stations (e.g., Blocks 4 and 6, Figure 3) and thus have wide posterior distributions.

3.2. Magnitude of the SSE

In all models, the amplitude of the slip can vary significantly, as seen in the distributions of the slip parameters (Figure S3). The equivalent magnitude, computed from the integrated slip over the whole surface and scaled by the shear modulus, is consistently about M_w6.1 and only varies among accepted models within a narrow range from M_w6.0 to 6.3 (95% bounds; Figure 3, inset); however, this is dependent on the choice of the shear modulus and the effect of varying the shear modulus is discussed in the supporting information. If we maintain this magnitude, but force all the patches to slip equally (an acceptable model within the confidence bounds, but not the "best" model from the distribution of slip parameters) the amount of slip on each patch would be ~0.2 m.

4. Strain Rate Modeling

Inversion of CGPS velocities for strain rate parameters is a useful tool to analyze the response of the volcanic edifice to stress induced by both volcanic and tectonic elements. We apply the technique first introduced by Haines and Holt (1993), improved by Holt and Haines (1995), and applied to volcanic areas by Bruno et al. (2012), to compute spatially continuous areal and shear strain rate. A detailed description of this approach is presented in Bruno et al. (2012). The areal strain rate (Figure 4a) shows dilatation around the upper part of the volcano, reaching values of about 6×10^{-13} s^{-1} in the summit craters. The large magnitude of the principal axes of average strain rates in the area between the altitude of 2,000 and 2,500 m asl, and their azimuthal distribution, confirms that the most deformed area (in the considered time span) is coincident with the main central craters of the volcano. This precludes any local source of inflation far from the summit area. Two zones of areal dilatation are also visible in the eastern flank of the volcano (Figure 4a): (1) the first, reaching values of about 6×10^{-13} s^{-1} (10^{-13} s^{-1} = 3.15 μstrain/yr), coincides with the TF; (2) the second, with values that do not exceed 4×10^{-13} s^{-1}, is located in the terminal part of the Mascalucia-Tremestieri-Trecastagni Fault (MTTF) System (the acronyms are described in Figure 1), near the coast, and elongated to the North up to the Acicatena-Valverde Fault (AVF). These zones of areal dilatation are related to the seaward slip of this sector of the volcano. This conclusion is supported by the azimuthal distribution of the principal axes of average strain rates, with the seaward directed maximum extension, which is consistent with the direction of the SSE. A slight areal contraction borders the summit area, with a preferred direction roughly N-S (Figure 4a).

Shear strain rate magnitudes (Figure 4b) indicate that the strike-slip component of deformation is present (i) in the NE Rift (with values reaching 1.4×10^{-13} s^{-1}), (ii) along the PFS, (iii) in the E-W direction (with values reaching 2.2×10^{-13} s^{-1}), and (iv) in the South Rift area (with magnitudes similar to the NE Rift), bordered to the West by the RF. The deformation shows strike-slip components also in the TFS, with values up to 1×10^{-13} s^{-1} (Figure 4b). We observe an area of clockwise rotation along the eastern flank that (Figure 4c) extends across the upper eastern flank and is bounded by the North-East Rift and the PF, the RNF scarps, and the TFS. East of the TFS, rotations reverse and an area of counterclockwise rotation is observed (Figure 4c). In the areas where the strike-slip component of deformation has been detected, low-magnitude seismic swarms have occurred (Figure 3b).

5. Interaction Stresses

We calculate the elastic stresses induced by each source that could possibly facilitate interactions between inflation and the SSE (Figure 3). We calculate the shear stresses produced by the reservoir inflation in the direction that would encourage flank slip. Conversely, we calculate the volumetric stresses as the trace of the stress tensor that are produced by the flank slip and could encourage inflation. However, neither produces stresses larger than a few kPa in the vicinity of the other sources, suggesting that elastic stress

transfer is a small but still possible influence. Since independent measurements of fluid changes correlated with SSEs were documented by Mattia et al. (2015), this work does not preclude the hypothesis of magma-derived fluids and the considerable influence fluids can have on fault slip.

We also calculate the effect of the slow slip on the larger known flank-bounding strike-slip faults (see Figure S7 in the supporting information). The largest stresses on the PF to the north of the mobile eastern flank of Mount Etna are about +0.3 MPa spanning from the coast to about 10 km inland, which encourages left-lateral slip. The 95% confidence bounds of the stresses determined from the posterior distribution of slips is from +0.13 to +4.3 MPa. The segments of the PF closest to the summit craters are not significantly affected by the slow slip. The region near the TFS is encouraged toward right-lateral slip with stresses of −0.2 to −0.3 MPa. The faults bounding the south side of the mobile eastern flank are minimally stressed by the slow slip.

6. Discussion and Conclusions

The inflation was coincident with flank motion between 11 December 2015 and 17 May 2016. The flank slip is similar but shallower than Kilauea's SSEs (Montgomery-Brown et al., 2009) and the majority of subduction zone SSEs. The lack of tectonic tremor observed during Mount Etna's SSEs is consistent with other shallow SSEs (e.g., Kilauea and Boso; Montgomery-Brown & Syracuse, 2015), yet those slip velocities tend to be faster. SSEs at Mount Etna are also not associated with swarms of regular small earthquakes like other shallow SSEs. The magnitude of the flank slip rate during this event is well constrained between M_w6.0 to 6.3. The distribution of the CGPS velocities indicates a process of inflation. The areal dilatation strain rate map confirms the presence of a nearly symmetrical inflation of the summit area (above 2,000–2,500 m asl). The shear strain rate map also highlights strike-slip style deformations along the PFS and the NE rift.

The shallow modeled planes, the coincidence with a period of intense inflation of the whole volcanic edifice (as previously found in 2009 and 2012, see Mattia et al., 2015), and that the inflating body does not result in significant shear stress that would encourage slip on the mobile flank suggest that the proposed model of fluid-induced SSEs observed at Mount Etna (Mattia et al., 2015) is supported by our analysis of CGPS data. We suggest that the source of the stresses that encourages SSEs at Mount Etna includes both gravitational spreading and tectonic forces but is facilitated by magmatic fluids.

The slip velocities for this event, on the order of 10^{-9} m/s, are slower than other global SSEs that lack tremor; however, there is high variability among global SSE velocities (Montgomery-Brown & Syracuse, 2015), and there are examples of shallow long-duration SSEs with slow velocities (e.g., New Zealand, Bartlow et al., 2014; Montgomery-Brown & Syracuse, 2015). The velocity differences and lack of tremor or seismic swarms directly related to slip along a decollement surface may be related to the significant influence of fluids in Mount Etna's flank.

Another remarkable result of this analysis is the demonstration of a stress induced by the slow slip in some of the fault systems, especially those on the eastern and north-eastern flanks of the volcano. The largest stresses are modeled on the PF, to the north of the mobile eastern flank of Mount Etna, encouraging left-lateral slip, while the area near the TFS is encouraged toward right-lateral slip. Hence, the stress and strain analyses from Mount Etna's CGPS network can be applied as a tool for seismic hazard analysis.

Acknowledgments
The original data analyzed here are available as a table in the supporting information. The authors thank the INGV-CT Gruppo Analisi Dati Sismici for providing earthquake data. The authors also thank three anonymous reviewers, and USGS reviewer K. Anderson for helpful comments. Any use of trade, firm, or product names is for descriptive purposes only and does not imply endorsement by the U.S. Government.

References

Aloisi, M., Bonaccorso, A., Gambino, S., Mattia, M., & Puglisi, G. (2003). Etna 2002 eruption imaged from continuous tilt and GPS data. *Geophysical Research Letters*, *30*(23), 2214. https://doi.org/10.1029/2003GL018896

Aloisi, M., Mattia, M., Ferlito, C., Palano, M., Bruno, V., & Cannavò, F. (2011). Imaging the multi-level magma reservoir at Mt. Etna volcano (Italy). *Geophysical Research Letters*, *38*, L16306. https://doi.org/10.1029/2011GL048488

Anderson, K., & Segall, P. (2013). Bayesian inversion of data from effusive volcanic eruptions using physics-based models: Application to Mount St. Helens 2004–2008. *Journal of Geophysical Research: Solid Earth*, *118*, 2017–2037. https://doi.org/10.1002/jgrb.50169.

Aster, R. C., Borchers, B., & Thurber, C. H. (2012). *Parameter estimation and inverse problems*. New York: Academic Press. https://doi.org/10.1016/S0074-6142(05)80014-2

Bartlow, N. M., Wallace, L. M., Beavan, R. J., Bannister, S., & Segall, P. (2014). Time-dependent modeling of slow slip events and associated seismicity and tremor at the Hikurangi subduction zone, New Zealand. *Journal of Geophysical Research: Solid Earth*, *119*, 734–753. https://doi.org/10.1002/2013JB010609

Bonforte, A., Guglielmino, F., Coltelli, M., Ferretti, A., & Puglisi, G. (2011). Structural assessment of Mount Etna volcano from Permanent Scatterers analysis. *Geochemistry, Geophysics, Geosystems*, *12*, Q02002. https://doi.org/10.1029/2010GC003213

Bruno, V., Ferlito, C., Mattia, M., Monaco, C., Rossi, M., & Scandura, D. (2016). Evidence of a shallow magma intrusion beneath the NE Rift system of Mt. Etna during 2013. *Terra Nova*, *28*(5), 356–363. https://doi.org/10.1111/ter.12228

Bruno, V., Mattia, M., Aloisi, M., Palano, M., Cannavò, F., & Holt, W. E. (2012). Ground deformations and volcanic processes as imaged by CGPS data at Mt. Etna (Italy) between 2003 and 2008. *Journal of Geophysical Research*, *117*, B07208. https://doi.org/10.1029/2011JB009114

Cervelli, P. (2013). Analytical expressions for deformation from an arbitrarily oriented spheroid in a half-space. Abstract V44C-06 Presented at the 2013 Fall Meeting, AGU, San Francisco, CA, 9–13 Dec.

Corsaro, R. A., Andronico, D., Behncke, B., Branca, S., Caltabiano, T., Ciancitto, F., … De Beni, E. (2017). Monitoring the December 2015 summit eruptions of Mt. Etna (Italy): Implications on eruptive dynamics. *Journal of Volcanology and Geothermal Research*, *341*, 53–69. https://doi.org/10.1016/j.jvolgeores.2017.04.018

Ferlito, C., Bruno, V., Salerno, G., Caltabiano, T., Scandura, D., Mattia, M., & Coltorti, M. (2017). Dome-like behavior at Mt. Etna: The case of the 28 December 2014 South East Crater paroxysm. *Scientific Reports*, *7*(1), 5361. https://doi.org/10.1038/s41598-017-05318-9

Haines, A. J., & Holt, W. E. (1993). A procedure for obtaining the complete horizontal motions within zones of distributed deformation from the inversion of strain rate data. *Journal of Geophysical Research*, *98*(B7), 12,057–12,082. https://doi.org/10.1029/93JB00892

Hastings, W. K. (1970). Monte Carlo sampling methods using Markov chains and their applications. *Biometrika*, *57*(1), 97–109. https://doi.org/10.1093/biomet/57.1.97

Herring, T. A., King, R. W., & McClusky, S. C. (2006). GAMIT reference manual. GPS Analysis at MIT, release, 10, 36.

Holt, W. E., & Haines, A. J. (1995). The kinematics of northern South Islands, New Zealand, determined from geologic strain rates. *Journal of Geophysical Research*, *100*, 17,991–18,010. https://doi.org/10.1029/95JB01059

Kreemer, C., Holt, W. E., Goes, S., & Govers, R. (2000). Active deformation in eastern Indonesia and the Philippines from GPS and seismicity data. *Journal of Geophysical Research*, *105*(B1), 663–680. https://doi.org/10.1029/1999JB900356

Mattia, M., Bruno, V., Caltabiano, T., Cannata, A., Cannavò, F., D'Alessandro, W., … Liuzzo, M. (2015). A comprehensive interpretative model of slow slip events on Mt. Etna's eastern flank. *Geochemistry, Geophysics, Geosystems*, *16*, 635–658. https://doi.org/10.1002/2014GC005585

Mattia, M., Montgomery-Brown, E. K., Bruno, V., & Scandura, D. (2016). A comparison of slow slip events at Etna and Kilauea volcanoes. Abstract EGU2016–4572 Presented at the EGU Meeting, Vienna, Austria, 17–22 April.

Mattia, M., Patane, D., Aloisi, M., & Amore, M. (2007). Faulting on the western flank of Mt Etna and magma intrusions in the shallow crust. *Terra Nova*, *19*(1), 89–94. https://doi.org/10.1111/j.1365-3121.2006.00724.x

Metropolis, N., Rosenbluth, A. W., Rosenbluth, M. N., Teller, A. H., & Teller, E. (1953). Equation of state calculations by fast computing machines. *The Journal of Chemical Physics*, *21*(6), 1087–1092. https://doi.org/10.1063/1.1699114

Monaco, C., Tappoiner, P., Tortorici, L., & Gillot, P. Y. (1997). Late Quaternary slip rates on the Acireale-Piedimonte normal faults and tectonic origin of Mt. Etna (Sicily). *Earth and Planetary Science Letters*, *147*, 125–139. https://doi.org/10.1016/S0012-821X(97)00005-8

Montgomery-Brown, E. K., Segall, P., & Miklius, A. (2009). Kilauea slow slip events: Identification, source inversions, and relation to seismicity. *Journal of Geophysical Research*, *114*, B00A03. https://doi.org/10.1029/2008JB006074

Montgomery-Brown, E. K., & Syracuse, E. M. (2015). Tremor-genic slow slip regions may be deeper and warmer and may slip slower than non-tremor-genic regions. *Geochemistry, Geophysics, Geosystems*, *16*, 3593–3606. https://doi.org/10.1002/2015GC005895

Okada, Y. (1985). Surface deformation due to shear and tensile fault in half-space. *Bulletin of the Seismological Society of America*, *75*, 1135–1154.

Palano, M. (2016). Episodic slow slip events and seaward flank motion at Mt. Etna volcano (Italy). *Journal of Volcanology and Geothermal Research*, *324*, 8–14. https://doi.org/10.1016/j.jvolgeores.2016.05.010

Palano, M., Rossi, M., Cannavò, F., Bruno, V., Aloisi, M., Pellegrino, D., … Mattia, M. (2010). Etn a geodetic reference frame for Mt. Etna GPS networks. *Annals of Geophysics*, *53*(4), 49–57. https://doi.org/10.4401/ag-4879

Schultz, R. A. (1995). Limits on strength and deformation properties of jointed basaltic rock masses. *Rock Mechanics and Rock Engineering*, *28*(1), 1–15. https://doi.org/10.1007/BF01024770

Segall, P. (2010). *Earthquake and volcano deformation*. Princeton: Princeton University Press. https://doi.org/10.1515/9781400833856

Williams, C. A., & Wadge, G. (1998). The effects of topography on magma chamber deformation models: Application to Mt. Etna and radar interferometry. *Geophysical Research Letters*, *25*(10), 1549–1552. https://doi.org/10.1029/98GL01136

Yang, X. M., Davis, P. M., & Dieterich, J. H. (1988). Deformation from inflation of a dipping finite prolate spheroid in an elastic half-space as a model for volcanic stressing. *Journal of Geophysical Research*, *93*(B5), 4249–4257. https://doi.org/10.1029/JB093iB05p04249